



Contents lists available at ScienceDirect



## Effect of temperature on the fatigue-crack growth behavior of the high-entropy alloy CrMnFeCoNi



Keli V.S. Thurston<sup>a,b</sup>, Bernd Gludovatz<sup>c,1</sup>, Anton Hohenwarter<sup>d</sup>, Guillaume Laplanche<sup>e</sup>, Easo P. George<sup>f,g</sup>, Robert O. Ritchie<sup>a,b,\*</sup>

<sup>a</sup> Materials Sciences Division, Lawrence Berkeley National Laboratory, Berkeley, CA, 94720, USA

<sup>b</sup> Department of Materials Science & Engineering, University of California, Berkeley, CA, 94720, USA

<sup>c</sup> School of Mechanical and Manufacturing Engineering, UNSW Sydney, NSW, 2052, Australia

<sup>d</sup> Department of Materials Physics, Montanuniversität Leoben and Erich Schmid Institute of Materials Science, Austrian Academy of Sciences, 8700, Leoben, Austria

<sup>e</sup> Institut für Werkstoffe, Ruhr-Universität Bochum, D-44801, Bochum, Germany

<sup>f</sup> Materials Science and Technology Division, Oak Ridge National Laboratory, Oak Ridge, TN, 37831, USA

<sup>g</sup> Department of Materials Science and Engineering, University of Tennessee, Knoxville, TN, 37996, USA

### ARTICLE INFO

**Keywords:**

High-entropy alloys  
Fatigue  
Crack propagation  
Temperature effects

### ABSTRACT

Near-equiatomic multi-component high-entropy alloys (HEAs) have engendered much attention of late due to the remarkable mechanical properties of some of these new metallic materials. In particular, one of the first reported HEAs, the equiatomic, single-phase, face-centered cubic (fcc) alloy CrMnFeCoNi, often termed the Cantor alloy, has been shown to display an exceptional combination of strength, ductility and fracture toughness, *i.e.*, damage tolerance, at room temperature, properties that are further enhanced at cryogenic temperatures. Despite this alloy being the most studied HEA to date, its resistance to crack growth under cyclic fatigue loading has not yet been characterized. Here, we examine its fatigue-crack propagation behavior, primarily at lower, near-threshold, growth rates, both at room temperature (293 K) and at 198 K. At 293 K, the alloy shows a fatigue threshold,  $\Delta K_{TH}$ , of  $\sim 4.8$  MPa $\sqrt{m}$ , which increases by more than 30% to  $\Delta K_{TH} \sim 6.3$  MPa $\sqrt{m}$  with decrease in temperature to 198 K; additionally, the Paris exponent  $m$  was found to increase from roughly 3.5 to 4.5 with decreasing temperature. Examination of the fracture surfaces and crack paths indicate a transition from predominantly transgranular crack propagation at room temperature to intergranular-dominated failure at the lower temperature. Such a change in crack path is generally associated with an increasing degree of physical contact between the two fracture surfaces, *i.e.*, roughness-induced fatigue crack closure, which is likely to be the main reason for the difference in the measured thresholds. Additionally, we believe that the higher thresholds found at 198 K are associated with the alloy's higher strength at lower temperatures, which both reduces the crack-tip opening displacements at a given stress-intensity range and prevents plastic deformations of the grains in the wake of the crack. At room temperature, such plastically deformed grains can be associated with a loss of contact shielding of the crack-tip through closure, resulting in a lower threshold compared to 198 K.

### 1. Introduction

Our society's demand for structural materials tailored to fit an increasingly wide range of applications, coupled with the development of a vast array of processing techniques, have spurred great interest in alloys that flout convention and may exhibit hitherto unknown yet desirable properties. The traditional standards of metallurgical design have tended to be limited to alloys consisting primarily of one or two base elements with additional alloying elements present in lower concentrations. However, the past decade has witnessed a significant

rise in interest focused on multiple-element alloys [1–7], in particular a suite of (near)-equiatomic metallic alloys that defy convention, consisting of five or more base metals able, under proper heat treatment, to form, at least in principle, a single phase with simple crystal structures [2,6–8]. These so-called 'high-entropy alloys' (HEAs) derive their name from the originally theorized role of the high configurational entropy in these materials to stabilize the observed phase(s) [5], although further studies have cast doubt on the role entropy plays in the stabilization of these materials [9–13]. To exclude any implications of the role entropy plays in these materials, the alloys are often alternatively termed 'multi-

\* Corresponding author. Materials Sciences Division, Lawrence Berkeley National Laboratory, Berkeley, CA, 94720, USA.  
E-mail address: [roritchie@lbl.gov](mailto:roritchie@lbl.gov) (R.O. Ritchie).

<sup>1</sup> Formerly at: Materials Sciences Division, Lawrence Berkeley National Laboratory, Berkeley, California 94720, USA.

principal element alloys' or 'complex concentrated alloys' [14]. Far from being mere curiosities though, high-entropy alloys and the related 'medium-entropy alloys' (MEAs; comprising 3 or 4 elements in near-equiatomic concentrations) are being examined in earnest as a class of seemingly unlimited new structural materials based on the belief that many new alloys with useful properties may be discovered [1–19].

A prominent sub-class of HEA and MEA alloys is based on the CrCoNi system. Indeed, the five-component equiatomic CrMnFeCoNi alloy, first described by Cantor in 2004 [1], is a single-phase face-centered cubic (fcc) solid solution with remarkable mechanical properties. Specifically, the alloy displays tensile strength levels of ~1 GPa associated with significant strain hardening, excellent ductility (~60–70%) and exceptional fracture toughness ( $K_{Jc} > 200 \text{ MPa}\sqrt{\text{m}}$ ) [2]; moreover, these properties tend to improve with decrease in temperature between ambient and 77 K [2,6,8,10,12], i.e., they display damage-tolerant properties that tend to run counter to the vast majority of metal alloys that show a propensity for increasingly brittle behavior at cryogenic temperatures [2,10,19,20].

Whereas good strength and toughness are invariably vital characteristics for a structural material, resistance to fatigue is often the limiting mechanical property, as this generally determines the engineering lifetime of a given component for many applications. As noted above, the mechanical properties of the CrMnFeCoNi alloy have been well characterized under monotonic loading [2,4,6,7,10,12,19], but there is little information to date how this alloy performs under cyclic loads. As a potential new class of structural materials, it is clearly important that the fatigue behavior of HEAs and the various factors that may affect it, such as grain size and temperature dependence, are clearly understood. To date there have been only a few studies on the fatigue of HEAs, but these have generally been focused on as-cast, rather than recrystallized materials with uniform grain size; moreover, they have all been performed at room temperature [21–23]. Our objective in this study is to characterize the high-cycle fatigue-crack propagation behavior of the CrMnFeCoNi alloy, using material with a uniform recrystallized grain size. Furthermore, as this alloy is particularly notable for its cryogenic damage-tolerant properties, we performed these experiments at both room temperature and 198 K, to evaluate how the improved strength, ductility and toughness of the material at cryogenic temperatures translates into its fatigue-crack growth resistance.

## 2. Experimental procedures

An ingot of the CrMnFeCoNi alloy was produced at the Ruhr-University, Bochum, through vacuum induction melting and casting into a cylindrical mold. The ingot was then sealed in a quartz tube and thermally homogenized at 1473 K for 48 h. Subsequently, the homogenized rod was rotary swaged at room temperature to reduce its diameter from 40 to ~16.5 mm before being recrystallized at 1073 K for 1 h, yielding a single-phase fcc material with a grain size of  $7 \pm 3 \mu\text{m}$  and a random orientation distribution [24]. The rod was then sliced into disc-shaped compact-tension (DC(T)) samples, in accordance with ASTM standard E1820 [25], using electrical discharge machining. 15 samples ( $n = 15$ ) were machined with a width,  $W$  of 12.5 mm and thickness,  $B$  of 6 mm; notches were cut with depths varying from  $a_o = 3.6\text{--}5.1 \mu\text{m}$ , corresponding to initial  $a_o/W$  ratios of ~0.28–0.4, respectively, and with notch root radii of ~100  $\mu\text{m}$ .

The faces of all samples were metallographically polished using silicon carbide paper to a final 1  $\mu\text{m}$  surface finish to allow accurate crack-length measurements on the surface of the samples using optical microscopy techniques. Additionally, an EA-SE-031DE-350 linear patterned strain gauge (Vishay Precision Group, Raleigh, NC, USA) was mounted to the back-face of each sample to allow monitoring of the crack length over the entire width of the sample during testing. Specifically, the crack lengths were determined from the unloading cycles using the compliance expression for the DC(T) sample with back-

face strain, as described by Ritchie et al. [26]:

$$\begin{aligned} a/W = & 0.796239 + 5.40205u - 103.821u^2 + 714.676u^3 - 2603.44u^4 \\ & + 4829.01u^5 - 3578.51u^6, \end{aligned} \quad (1)$$

$$\text{where } u = \frac{1}{\sqrt{-EBCW} + 1}. \quad (2)$$

Here  $E$  corresponds to the Young's modulus of the material, and  $C$  represents the compliance calculated as the reciprocal from the unloading slope of the samples during testing. This calibration is considered valid for the range  $0.3 \leq a/W \leq 0.8$ ; all samples were within this range for the entire duration of testing to ensure measurement validity.

Before testing, all samples were fatigue pre-cracked in ambient conditions using an electro-servo hydraulic MTS testing machine (MTS Corporation, Eden Prairie, MN, USA) controlled by an Instron 8800 digital controller (Instron Corporation, Norwood, MA, USA). Fatigue pre-cracking was conducted under load control (tension-tension loading) within a stress-intensity range,  $\Delta K = K_{\max} - K_{\min}$ , between 8 and 10 MPa $\sqrt{\text{m}}$  at a constant sinusoidal frequency,  $f$ , of 25 Hz and a load ratio,  $R = 0.1$ , where  $R$  is the ratio of minimum to maximum load. The back-face strain gauges were calibrated and balanced at zero-load to ensure residual strains from mounting would not affect crack-length measurement, which was further verified during pre-cracking by optically checking both sides of the samples for crack length and linearity. Final overall pre-crack lengths including notches ranged from  $a = 3.7 \text{ mm--}5.17 \text{ mm}$  ( $a/W \sim 0.3\text{--}0.41$ ), all in accordance with ASTM E647 [27].

Actual fatigue-crack growth tests were performed under cyclic loading at  $f = 25 \text{ Hz}$  (sine wave) at a constant load ratio of  $R = 0.1$  at both room temperature air (293 K) and in a dry ice/ethanol bath (198 K). Near-threshold crack-growth rates were determined under load-shedding conditions, which were automated to decrease the load at a rate such that the normalized  $K$ -gradient remains above  $-0.08 \text{ mm}^{-1}$ , as recommended in ASTM E647 [27].  $\Delta K_{\text{TH}}$  fatigue threshold stress-intensity values were determined as the maximum value of the stress-intensity range,  $\Delta K$ , to give a growth rate approaching  $10^{-11} \text{ m/cycle}$ . Higher growth rates were measured under constant alternating load conditions. To obtain cryogenic test conditions, a dry ice/ethanol bath was prepared and maintained at 198 K for the duration of the test. Samples subjected to 198 K conditions were tested in a continuous manner at this temperature to avoid potential thermal cycling effects [28]. For all samples, crack length verification by optical microscopy was carried out after testing.

To determine the microstructural mechanisms controlling the propagation of the fatigue cracks in this alloy and to investigate the nature of the crack paths, some samples were sliced longitudinally through the center for back-scattered electron (BSE) and electron backscatter diffraction (EBSD) analyses, performed using a Zeiss LEO 1525 field-emission scanning electron microscope (FE-SEM, Carl Zeiss, Oberkochen, Germany) operated at 20 kV using a TEAM™ EDAX analysis system (Ametek EDAX, Mahwah, NJ, USA). To perform fractography analyses, samples from both temperatures were subsequently quasi-statically loaded to complete failure to have unrestricted access to their fracture surfaces. In addition to the microscopic analysis with the Zeiss-SEM, fracture surface characterization was also performed using a JSM-7500F SEM (JEOL USA, Arvada, CO, USA) operated at 5–15 kV in secondary electron, SE, mode.

## 3. Results and discussion

Prior studies conducted on the equiatomic, single-phase fcc CrMnFeCoNi alloy with the same microstructure have found it to display mechanical properties that either remain consistent or improve as the testing temperature is lowered into the cryogenic regime. In this regard, both strength and ductility of the material are particularly

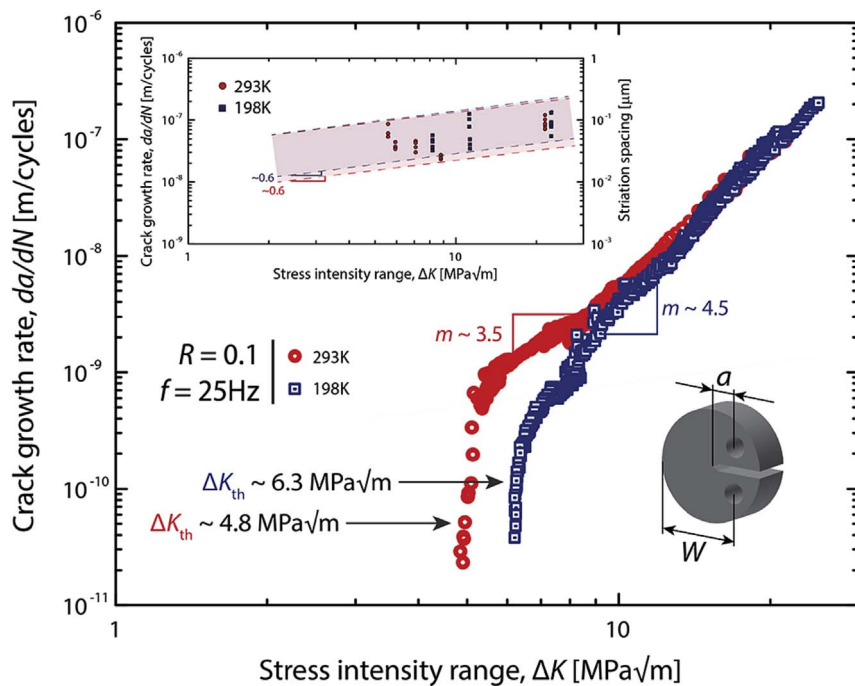


**Fig. 1.** Fatigue-crack growth behavior of the CrMnFeCoNi alloy, tested at a load ratio  $R$  of 0.1 at 293 K and 198 K. A direct comparison of the fatigue-crack growth curves, as a function of the stress-intensity range,  $\Delta K$ , at both temperatures tested on disc-shaped compact-tension (DC(T)) samples at a frequency of  $f = 25$  Hz reveal a clear shift in the fatigue threshold, increasing some 30%, from  $\sim 4.8$  MPa $\sqrt{m}$  to  $\sim 6.3$  MPa $\sqrt{m}$ , as the temperature was reduced from ambient to cryogenic conditions. The Paris exponent  $m$  was found to change from 3.5 at 293 K to 4.5 at 198 K. The smaller sized, solid symbols in the inset indicate the corresponding variation, as a function of  $\Delta K$ , in local crack-growth rates, which were estimated from striation spacing measurements on the scanning electron microscopy images of the fracture surfaces.

notable for their strong temperature dependence; the transition from 293 K to 198 K yields an increase in ultimate tensile strength from  $\sim 760$  MPa to  $\sim 925$  MPa with a similar increase in yield strength from  $\sim 410$  MPa to  $\sim 520$  MPa while its ductility increases from  $\sim 0.6$  to  $\sim 0.7$  [2]. Over the same temperature range, the Young's modulus [29,30], toughness and strain hardening exponent remain relatively unchanged with both the Young's modulus,  $E$ , and fracture toughness,  $K_{Jc}$ , increasing marginally from 202 GPa to 209 GPa and from 217 MPa $\sqrt{m}$  to 221 MPa $\sqrt{m}$ , respectively; the strain hardening exponent of the material, however, remains consistently high at  $\sim 0.4$  [2]. These trends, displayed by strength, modulus, toughness and strain hardening coefficient, have been found to continue as the temperature is further decreased to 77 K.

Here, the fatigue-crack growth rates,  $da/dN$ , of the alloy, for tests at 293 K in air and at 198 K in dry ice/ethanol, are plotted in Fig. 1 as a function of the applied stress-intensity range,  $\Delta K$ . Although crack-propagation rates are comparable in the mid-range of growth rates above  $\sim 10^{-8}$  m/cycle with only a modest change of the Paris exponent  $m$  from 3.5 at 293 K to 4.5 at 198 K, near-threshold growth rates and the value of the fatigue threshold,  $\Delta K_{TH}$ , of this alloy are markedly improved at cryogenic temperatures. Specifically, growth rates are lowered by up to an order of magnitude, and threshold  $\Delta K_{TH}$  values are increased by  $\sim 30\%$ , from  $\sim 4.8$  MPa $\sqrt{m}$  to  $\sim 6.3$  MPa $\sqrt{m}$ , with decrease in temperature from 293 K to 198 K.<sup>2</sup>

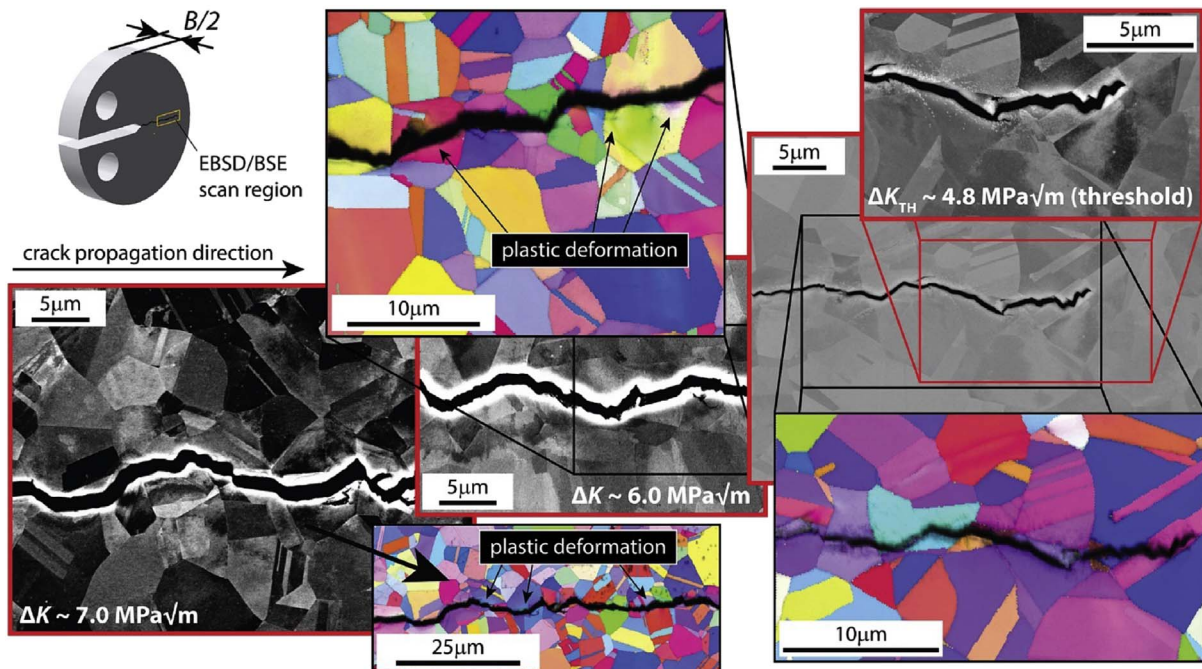
### 3.1. Crack path studies

Examination of the crack paths was performed by sectioning samples at mid-thickness. Near the threshold and at higher growth

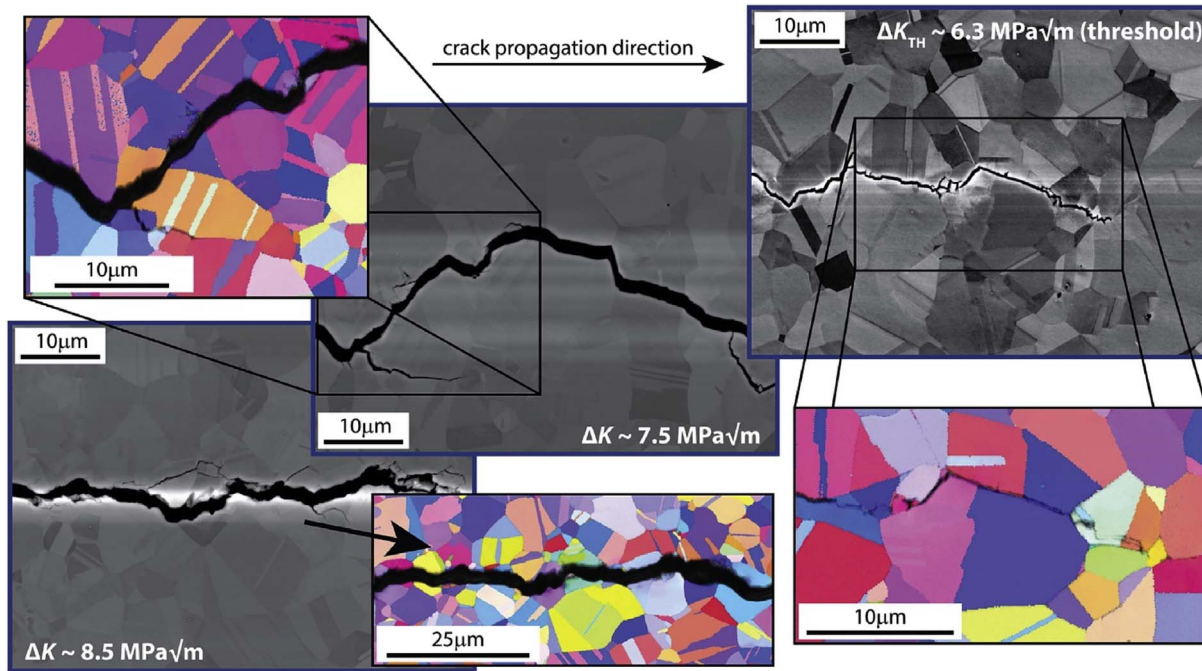
rates at room temperature, the crack paths are mainly transgranular with some minor intergranular crack growth at low and intermediate growth rates, as is apparent from the BSE images and EBSD scans in Fig. 2. The BSE images of the crack-tip region near the threshold at  $\Delta K = 4.8$  MPa $\sqrt{m}$  clearly indicate that the propagating crack runs through the grains and recrystallization twins and not along their boundaries. EBSD images taken from the wake of the crack at  $\Delta K$  values of  $\sim 6.0$  MPa $\sqrt{m}$  and  $\sim 7.0$  MPa $\sqrt{m}$  show significant amounts of plastic deformation in the grains neighboring the crack flanks partly resulting from geometrically-necessary dislocations emitted from the crack tip during loading and unloading of the samples. Additionally, such plastically-deformed regions naturally occur as a result of local deviations from a straight crack path leading to physical contact of the mating crack surfaces resulting from small variations in the mode II displacements of the neighboring crack flanks. This is known as roughness-induced fatigue crack closure and acts to lower the crack-driving force experienced at the tip of the growing crack by effectively increasing the value of the minimum stress intensity in the fatigue cycle [31,32]. At room temperature, where the alloy has a lower strength compared to at 198 K, such closure can result in local plastically deformed regions near the propagated crack and particularly of the individual grains next to the crack flanks. In a material where the ambient-temperature yield strength is relatively low, such physical contact of the mating crack surfaces has the potential to slightly flatten the crack path locally thereby causing a partial loss of contact shielding and allowing the crack to grow marginally faster as compared to that at lower temperatures where the yield strength is higher [33]. We believe that this mechanism accounts to a large extent for the difference found in the fatigue threshold shown in Fig. 1. Interestingly, despite the high stresses near the crack tip, deformation induced nano-scale twinning could not be observed by BSE and EBSD microscopy at room temperature.

Fig. 3 displays the crack paths of the fatigue cracks at 198 K. Note that akin to the behavior at 293 K, we could not see evidence of

<sup>2</sup> The Paris exponent  $m$  is defined by the slope of the  $da/dN$  vs.  $\Delta K$  curve in the mid-growth rate regime which can be described by the simple Paris power-law,  $da/dN = C \Delta K^m$ . The constants  $C$  for this linear mid-growth regime were computed to be  $1.9 \times 10^{-6}$  and  $9.7 \times 10^{-8}$  [units: m.cycle $^{-1}$  (MPa $\sqrt{m}$ ) $^{-m}$ ] at 293 K and 198 K, respectively.



**Fig. 2.** Crack path characterization of the CrMnFeCoNi alloy fatigue tested at 293K. Back-scattered electron (BSE) images and electron back-scatter diffraction (EBSD) scans taken at the mid-thickness of the samples near the threshold at  $\Delta K = 4.8 \text{ MPa}\sqrt{\text{m}}$ , specifically from the wake of the crack at  $\Delta K$  values of  $\sim 6$  and  $\sim 7 \text{ MPa}\sqrt{\text{m}}$ , clearly show transgranular fracture as the dominant crack propagation mode. Images taken at the crack tip indicate that the crack propagated through the grains and recrystallization twins and not along their boundaries. EBSD scans taken from the wake of the propagating crack show plastically deformed region along the crack flanks resulting from physical contact between the mating crack surfaces and the lower strength of the alloy at room temperature.



**Fig. 3.** Crack path characterization of the CrMnFeCoNi alloy fatigue tested at 198 K. In contrast to the behavior at room temperature (Fig. 2), both BSE images and EBSD scans revealed intergranular fracture as the dominant crack propagation mechanism at 198 K. The boundaries of the recrystallization twins do not appear to influence the path of the crack tip, as can be seen near the threshold at  $\Delta K = 6.3 \text{ MPa}\sqrt{\text{m}}$  and at higher growth rates at  $\Delta K$  values of  $\sim 7.5 \text{ MPa}\sqrt{\text{m}}$  and  $\sim 8.5 \text{ MPa}\sqrt{\text{m}}$ ; this is believed to be a result of the higher strength of the material at 198 K, such that plastically deformed regions along the propagated crack do not occur.

nanoscale deformation twinning associated with the crack-growth mechanisms in our BSE and EBSD analyses. However, compared to the room-temperature behavior, both BSE images and EBSD scans clearly show significant amounts of intergranular fracture at this lower temperature; as at room temperature though, the presence of recrys-

tallization twins did not appear to influence the crack trajectory. As a result of the intergranular crack propagation at the lower temperatures, the local crack path was naturally more deviated compared to that at room temperature, thereby giving rise to significantly more contact of the neighboring crack flanks to promote roughness-induced crack

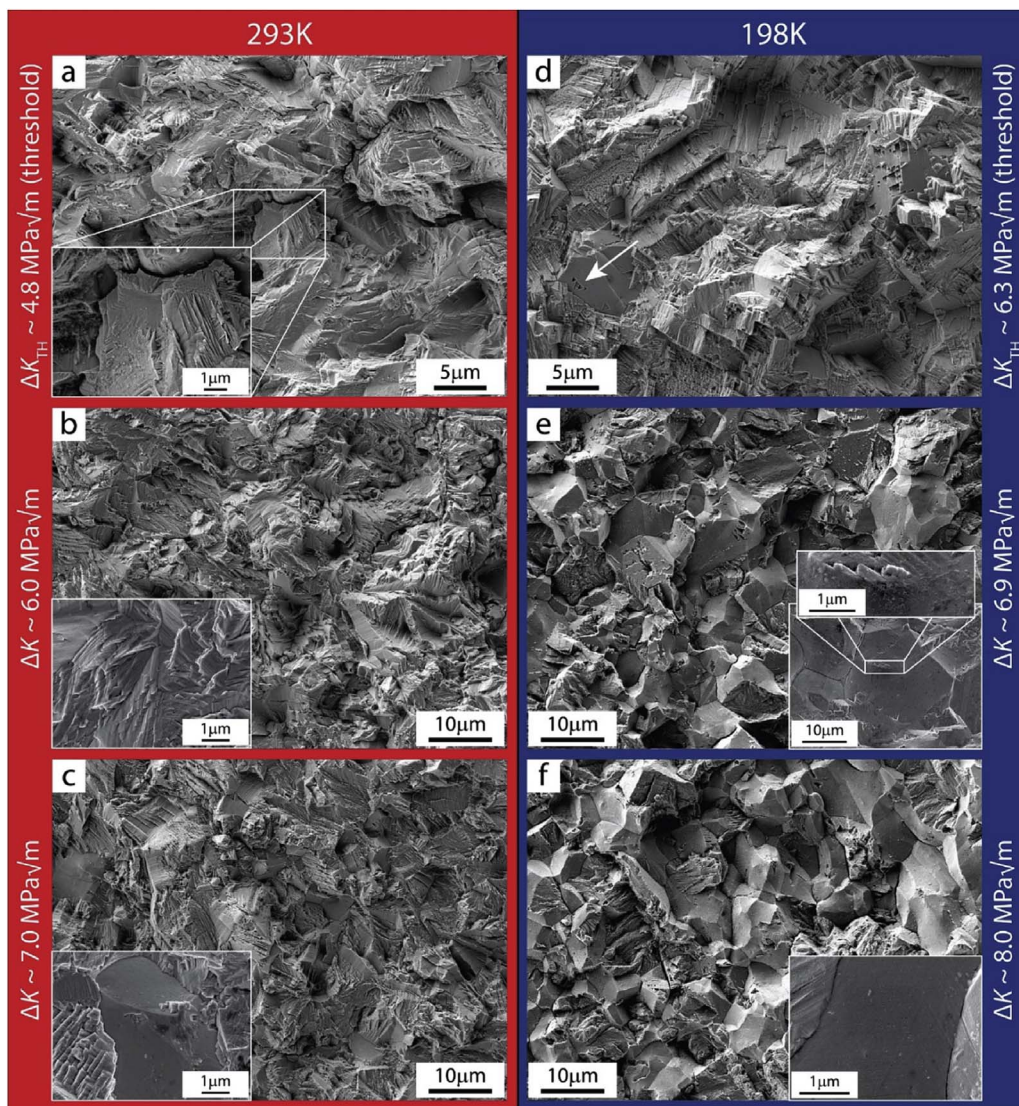


**Fig. 4. Fractographic analysis of CrMnFeCoNi samples tested at 293 K and 198 K.** Fracture surface characterization of samples tested at 293 K show mainly intergranular crack propagation (a–c) with some minor transgranular failure regions (inset of (c)). The highly-serrated fracture surface features covering most of the intergranular failure region (insets of (b) and (c)) are likely associated with cyclic slip steps resulting from dislocation motion by planar slip [6]). Similar features in the near-threshold region at 198 K (d) appear to also result from planar slip as the major deformation mechanism at this temperature. At higher growth rates (e,f) crack propagation occurs mainly through intergranular fracture. The white arrow in (d) and the insets of (e) indicate polyhedral features that likely show the ends of recrystallization twins formed perpendicular to the grain boundaries into the grains during processing of the material.

closure; this is consistent with the 30% higher threshold at 198 K,  $\Delta K = 6.3 \text{ MPa}\sqrt{\text{m}}$ , as compared to  $\Delta K = 4.8 \text{ MPa}\sqrt{\text{m}}$  at 293 K,<sup>3</sup> this crack closure mechanism operates particularly effectively within low stress-intensity range conditions like those of the near-threshold region [34,35]. where the fracture surface asperities, that act to wedge the crack, are comparable in size to the crack-tip opening displacements. Additionally, the higher strength at the lower temperature acts to limit these crack-tip opening displacements at a given  $\Delta K$ , as this displacement is proportional to  $\Delta K^2/\sigma_y E$ , where  $\sigma_y$  is the flow strength and  $E$  the Young's modulus; correspondingly, the generation of new crack surface during the opening of the crack in each cycle will be less effective.

<sup>3</sup> It should be noted that while room-temperature testing was conducted in ordinary ambient air (relatively moist environment), testing at 198 K was performed in a relatively moisture-free inert liquid, thereby raising the question whether oxide-induced crack closure [28,34] can play an additional role in explaining the differences in fatigue resistance at the two temperatures. However, this closure mechanism cannot explain the increased threshold at lower temperatures as one would expect to see an opposite trend, with the humid air generating thicker oxide films at 293 K and hence a higher threshold, than in dry ice/ethanol at 193 K [34].

### 3.2. Fractography

As can be expected from the BSE images and EBSD scans shown in Fig. 2, SEM characterization of the fracture surfaces of samples fatigued at 293 K revealed mainly transgranular crack propagation (Fig. 4a–c) with some minor intergranular failure regions (inset of Fig. 4c). Most of the transgranular failure region is covered with highly serrated fracture surface features at both the threshold (Fig. 4a) and at higher growth rates (Fig. 4b and c). The serrations on the fracture surfaces are clearly different in size and shape than typical striations which were found at higher growth rates, as described below; they have far sharper edges (insets Fig. 4a–c) and appear to form at specific angles with respect to each other (insets Fig. 4a,c). Given that at room temperature, nanoscale deformation twinning has not been found as dominant deformation mechanism in this alloy in both strength and fracture toughness tests [2,6,36], the latter having significantly higher distributions of crack-tip stresses than those generated during fatigue-crack growth, these periodic serrations cannot be attributed to twinning as the prominent deformation mechanism occurring at the crack tip. Instead, they can

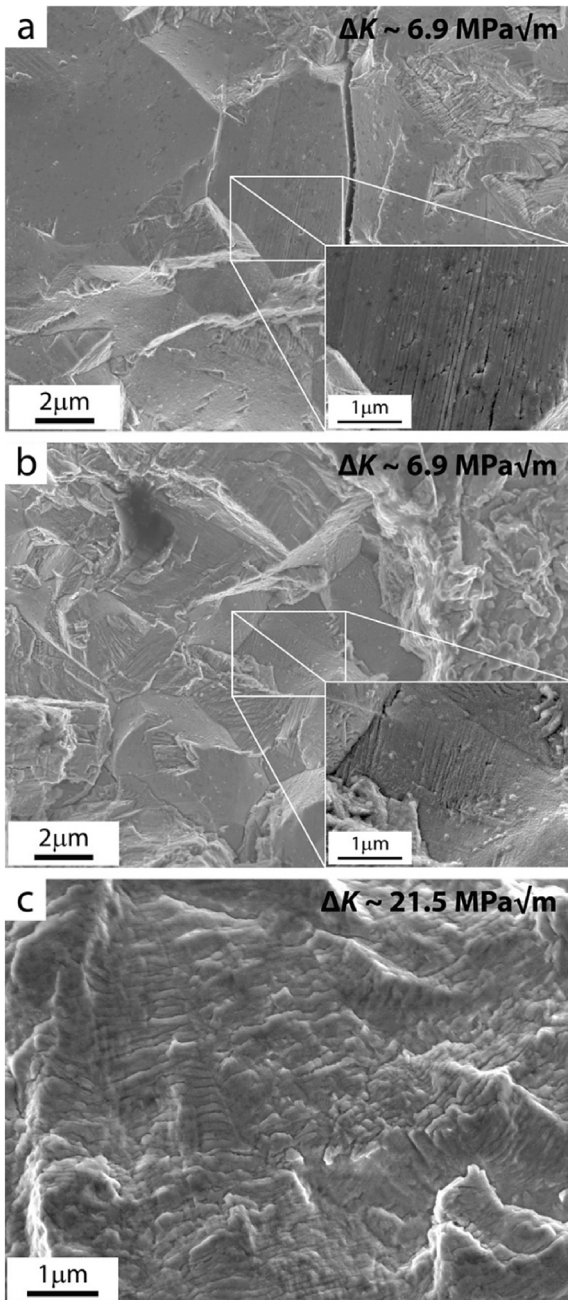


**Fig. 5. Characterization of fracture surface of samples tested at 198 K.** Slip steps that have formed parallel to grain boundaries are shown as serrated straight lines, as shown in (a) and the inset of (a). At the same growth rate at  $\Delta K \sim 6.9 \text{ MPa}\sqrt{\text{m}}$ , fatigue striations and slip steps can be found on the fracture surface (b) and the inset of (b)). At  $\Delta K \sim 21.5 \text{ MPa}\sqrt{\text{m}}$  the spacing of fatigue striations corresponds well to the macroscopic growth rate of  $\sim 10^{-7} \text{ m/cycle}$  (c).

only be associated with cyclic slip steps resulting from dislocation motion by planar slip which has been confirmed as the main deformation mechanism for the material at this temperature [6].

Similar to the fracture morphology at 293 K, the fracture surface in the near-threshold region at 198 K, at  $\Delta K = 6.3 \text{ MPa}/\text{m}$ , is highly serrated with sharp edges that form at specific angles, as shown in Fig. 4d, indicating that planar slip is also a major deformation mechanism at this temperature. Crack propagation at higher growth rates occurred mainly through intergranular failure, as shown in Fig. 4e and f and the inset of Fig. 4f, consistent with the BSE images and EBSD scans shown in Fig. 3. Interestingly, polyhedral features can be found on numerous grain boundaries, as indicated by the white arrow in

Fig. 4d and the insets of Fig. 4e; we believe that these features are the ends of recrystallization twins formed perpendicular to the grain boundaries during processing of the alloy. In addition, some of the grain boundaries show serrated straight lines, see Fig. 5a, which appear to be the edges of the planes of dislocations forming slip steps on the grain boundaries. Akin to the room temperature tests and consistent with both BSE images and EBSD scans, nanoscale deformation twins have not been found on the fracture surfaces of the samples tested at 198 K.

### 3.3. Striation spacing analysis

At higher growth rates, traditional fatigue striations are visible on the fatigue fracture surfaces of this high-entropy alloy (Fig. 5c). Unlike the periodic markings discussed above, which portray sharp features characteristic of planar slip, these features are more rounded and characteristic of ductile striations. To analyze these features, we have screened the fracture surfaces of four samples specifically for fatigue striations, two each from the 198 K and 293 K crack-growth experiments. Sampling was conducted at intervals of 1 mm, beginning 1 mm from the notch along the width of the sample until the overload region along the centerline of the sample, with multiple images taken at each location to check for consistency. While the fatigue striations at growth rates near the threshold are hard to detect and cannot often be easily distinguished from slip steps, e.g., see Fig. 5b, careful investigation of the fatigue striations, as shown on the example of a sample tested at  $\Delta K \sim 21.5 \text{ MPa}\sqrt{\text{m}}$  (Fig. 5c) shows good agreement (Fig. 1) between their spacing and the macroscopic growth rate of  $\sim 10^{-7} \text{ m/cycle}$  for both temperatures, as shown in the inset of Fig. 1. The inset of Fig. 1 also clearly indicates the actual correspondence of striation spacing as a function of  $\Delta K$  of the local crack-growth rates and the macroscopic growth rates measured at both temperatures. At lower values of  $\Delta K$ , the width of fatigue striations begins to diverge from the macroscopic growth rates, behavior which is indicative of the non-uniform crack propagation along the crack front at low growth rates as the crack advances in an incremental fashion. Overall, striation spacing measurements for both sets of samples displayed the generally linear trend characteristic of the approximate first-order description of macroscopic crack-growth rate behavior, albeit with scatter due to variability in measurements.

### 3.4. Comparison to other alloys

Based on the previously reported mechanical properties of the CrMnFeCoNi alloys in combination with its fatigue performance shown in this study, the alloy demonstrates high potential as a structural material for engineering applications, especially at lower temperatures [2].

Compared to other HEAs, austenitic stainless steels and twinning-induced plasticity (TWIP) steels, all tested at 298 K at similar testing conditions and comparable in terms of microstructure, the Cantor alloy shows excellent fatigue crack-growth performance at both 298 K and 198 K, as shown in Fig. 6; details about the individual materials and testing conditions can be found in Table 1. The fatigue-crack growth behavior of the CrMnFeCoNi alloy bore the most similarity to that of TWIP steels [36,37]. Akin to our material, TWIP steels also have displayed a lack of twinning behavior under fatigue conditions at room temperature [36,37]. However, they are also known for their high strength complemented with large ductility attributed to their propensity towards deformation twinning at lower temperatures [38]. As shown in Fig. 6, both their fatigue thresholds and their Paris slopes are comparable to our materials. Furthermore, the CrMnFeCoNi alloy compares favorably in terms of its fatigue threshold to several widely used high-strength steels of both low and moderate carbon content with comparable strength although crack-growth rates in the Paris regime are invariably fairly similar [39–41]. In contrast, the Cantor alloy

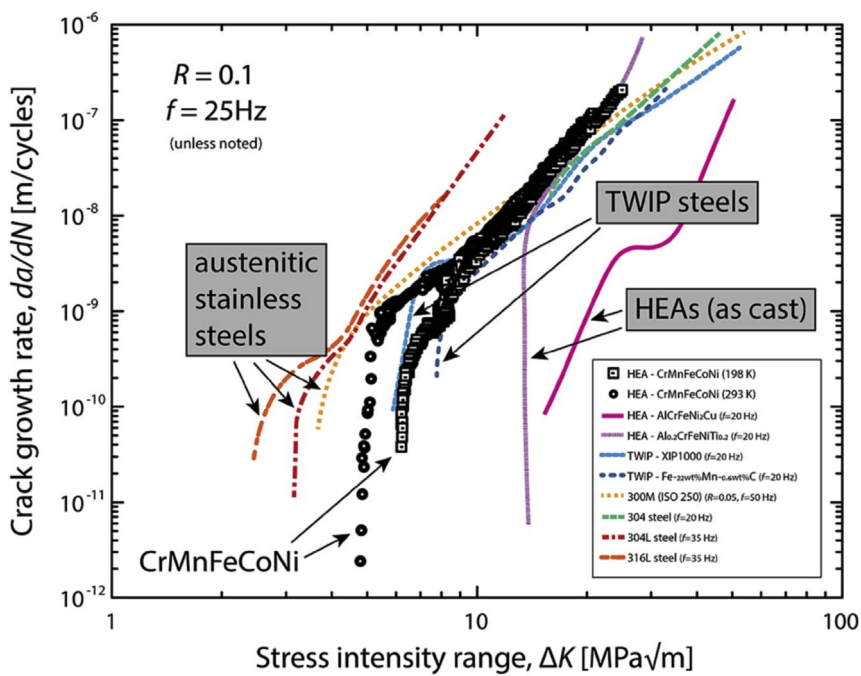


**Fig. 6. Comparison of the fatigue-crack growth behavior of the CrMnFeCoNi high-entropy alloy with austenitic stainless steels and TWIP steels (at 293 K unless otherwise noted).** The Cantor alloy displays fatigue behavior most similar to twinning-induced plasticity (TWIP) [36,37] and quenched and tempered low-alloy steels [38]. Austenitic stainless steels with comparable microstructure show slightly lower threshold with similar Paris slopes of  $\sim 3.5\text{--}4.5$  [40,41]. The Al-containing HEAs demonstrated both higher Paris-regime slopes and fatigue thresholds [21], which may be attributed largely to the as-cast microstructure in combination with the small sample sizes that were used during testing.

displayed a lower fatigue threshold to the related Al-containing HEAs [21,22], but the reason for the disparity may be due to the differences in microstructure between the alloys, particularly between the as-cast structure of the Al-based HEAs and the uniformity of our  $\sim 7\text{ }\mu\text{m}$  grain size CrMnFeCoNi, rather than due to inherent compositional differences. As-cast structures have been found to exhibit higher fatigue thresholds than their more finely grained counterparts, which is linked to an increased fracture surface roughness [42]. Moreover, we believe that the initially published fatigue data [21] on the Al-CrFeNi-based HEAs may be in error, in terms of unacceptably high fatigue threshold values above  $20\text{ MPa}\sqrt{\text{m}}$ , due to the small size of the specimens tested and the correspondingly excess plasticity throughout their cross-sections. Data on these Al-containing HEA using larger specimen size, in comparison to the extent of local plasticity, should resolve this issue.

#### 4. Conclusions

The equiatomic, single-phase, face-centered cubic high-entropy alloy CrMnFeCoNi has been investigated with respect to its fatigue crack-propagation properties at both room temperature and 198 K. The following specific conclusions can be made:

- The alloy was found to display a fatigue threshold,  $\Delta K_{\text{TH}}$  of  $\sim 4.8\text{ MPa}\sqrt{\text{m}}$  at room temperature which increased to  $\Delta K_{\text{TH}} \sim 6.3\text{ MPa}\sqrt{\text{m}}$  at 198 K; the Paris exponent  $m$  was relatively unchanged at both temperatures and found to be roughly between 3.5 and 4.5.
- At room temperature, fatigue-crack propagation was associated predominantly with transgranular fracture where physical contact of the mating crack surfaces results in plastic deformation of grains near the crack flanks thereby reducing the contact area of neighboring fracture surfaces. At cryogenic temperatures, intergranular fracture is the dominating crack propagation mode resulting in pronounced physical contact of the neighboring crack flanks resulting in enhanced roughness-induced fatigue crack closure.
- Fatigue fracture surfaces at room temperature showed highly serrated fracture surface features along the entire crack path indicating cyclic slip steps resulting from planar dislocation slip, the main deformation mechanism at this temperature. At 198 K, fatigue fracture surfaces in the threshold region appeared identical to the room temperature tests. The fracture surfaces of samples tested in the Paris regime showed largely intergranular failure; the resulting rougher fracture morphologies likely created higher levels

**Table 1**

Comparison of fatigue crack growth testing parameters and results for data shown in Fig. 6.

Alloy	R (load ratio)	Frequency [Hz]	Grain Size [ $\mu\text{m}$ ]	Young's Modulus [GPa]	Paris slope [m]	Threshold [MPa $\sqrt{\text{m}}$ ]	$\Delta K_{\text{TH}}/\text{E} [\sqrt{\text{m}}]$
HEA - CrMnFeCoNi (293 K)	0.1	25	7	202	3.5	4.8	0.024
HEA - CrMnFeCoNi (198 K)	0.1	25	7	210	4.5	6.3	0.030
HEA - AlCrFeNi <sub>2</sub> Cu [21]	0.1	20	as-cast	<sup>a</sup>	3.4	17	—
HEA - Al <sub>0.2</sub> CrFeNi <sub>0.2</sub> [21]	0.1	20	as-cast	<sup>a</sup>	4.9	16	—
XIP 1000-TWIP steel [36]	0.1	20	2	188	2.7	5.9	0.031
Fe-22 wt% Mn-0.6 wt% C TWIP steel [37]	0.1	20	5	<sup>a</sup>	3.8	7.6	—
300-M steel (ISO250) [39]	0.05	50	20	205	2.5	3.6	0.018
304 steel [40]	0.1	20	<sup>a</sup>	200	3.8	15.8	0.079
304L steel [41]	0.1	35	40	193	5.8	4.8	—
316L steel [41]	0.1	35	38	193	4.9	3.3	—

<sup>a</sup> Values not reported in the corresponding literature.

of roughness-induced crack closure which contributed to the higher  $\Delta K_{TH}$  threshold values at the lower temperature. Fatigue striations present on both sets of fracture surfaces followed a first-order description of crack-growth behavior with nominal agreement between striation width and crack growth rate at higher growth rates and the expected divergence at decreasing stress-intensity ranges.

- Considering testing conditions and microstructure, the Cantor alloy compares favorably in terms of its fatigue-crack growth resistance to austenitic stainless steels and TWIP steels. Taken with its remarkable combination of strength, ductility and fracture toughness at both ambient and cryogenic temperatures, the high-entropy alloy CrMnFeCoNi represents an impressive structural material with many potential applications that can utilize its impressive damage-tolerant properties.

## Acknowledgments

This research was supported at the Lawrence Berkeley National Laboratory (via the Mechanical Behavior of Materials Program, KC13) and the Oak Ridge National Laboratory by the U.S. Department of Energy, Office of Science, Office of Basic Energy Sciences, Materials Sciences and Engineering Division. G.L. acknowledges funding from the German Research Foundation (DFG) through project LA 3607/1-1.

## References

- B. Cantor, I.T.H. Chang, P. Knight, A.J.B. Vincent, Microstructural development in equiatomic multicomponent alloys, *Mater. Sci. Eng. A* 375–377 (2004) 213–218, <http://dx.doi.org/10.1016/j.mesa.2003.10.257>.
- B. Gludovatz, et al., A fracture-resistant high-entropy alloy for cryogenic applications, *Science* 345 (2014) 1153–1158, <http://dx.doi.org/10.1126/science.1254581>.
- M.J. Yao, K.G. Pradeep, C.C. Tasan, D. Raabe, A novel, single phase, non-equiatomic FeMnNiCoCr high-entropy alloy with exceptional phase stability and tensile ductility, *Scr. Mater.* 72–73 (2014) 5–8, <http://dx.doi.org/10.1016/j.scriptamat.2013.09.030>.
- B. Gludovatz, E.P. George, R.O. Ritchie, Processing, microstructure and mechanical properties of the CrMnFeCoNi high-entropy alloy, *JOM J. Min. Met. Mat. S.* 67 (2016) 2262–2270, <http://dx.doi.org/10.1007/s11837-015-1589-z>.
- J.W. Yeh, et al., Nanostructured high-entropy alloys with multiple principle elements: novel alloy design concepts and outcomes, *Adv. Eng. Mater.* 6 (2004) 299–303, <http://dx.doi.org/10.1002/adem.200300567>.
- F. Otto, et al., The influences of temperature and microstructure on the tensile properties of CoCrFeMnNi high-entropy alloy, *Acta Mater.* 61 (2013) 5743–5755, <http://dx.doi.org/10.1016/j.actamat.2013.06.018>.
- N. Stepanov, et al., Effect of cryo-deformation on structure and properties of CoCrFeNiMn high-entropy alloy, *Intermetallics* 55 (2015) 8–17, <http://dx.doi.org/10.1016/j.intermet.2014.12.004>.
- F. Otto, et al., Decomposition of the single-phase high-entropy alloy CrMnFeCoNi after prolonged anneals at intermediate temperatures, *Acta Mater.* 112 (2016) 40–52, <http://dx.doi.org/10.1016/j.actamat.2016.04.005>.
- E.J. Pickering, N.G. Jones, High-entropy alloys: a critical assessment of their founding principles and future prospects, *Int. Mater. Rev.* 61 (2016) 1743–2804, <http://dx.doi.org/10.1080/09506608.2016.1180020>.
- F. Otto, Y. Yang, H. Bei, E.P. George, Relative effects of enthalpy and entropy on the phase stability of equiatomic high-entropy alloys, *Acta Mater.* 61 (2013) 2628–3263, <http://dx.doi.org/10.1016/j.actamat.2013.01.042>.
- N.G. Jones, J.W. Aveson, A. Bhowmik, B.D. Conduit, H.J. Stone, On the entropic stabilization of an  $Al_{0.5}CrFeCoNiCu$  high entropy alloy, *Intermetallics* 54 (2014) 148–153, <http://dx.doi.org/10.1016/j.intermet.2014>.
- C.C. Tasan, Y. Deng, K.G. Pradeep, M.J. Yao, H. Springer, D. Raabe, Composition dependence of phase stability, deformation mechanisms, and mechanical properties of the CoCrFeMnNi high-entropy alloy system, *JOM J. Min. Met. Mat. S.* 66 (2014) 1993–2001, <http://dx.doi.org/10.1007/s11837-014-1133-6>.
- D. Ma, B. Grabowski, F. Körmann, J. Neugebauer, D. Raabe, Ab initio thermodynamics of the CoCrFeMnNi high entropy alloy: importance of entropy contributions beyond the configurational one, *Acta Mater.* 100 (2015) 90–97, <http://dx.doi.org/10.1016/j.actamat.2015.08.050>.
- D.B. Miracle, O.N. Senkov, A critical review of high entropy alloys and related concepts, *Acta Mater.* 122 (2017) 448–511, <http://dx.doi.org/10.1016/j.actamat.2016.08.081>.
- J.W. Yeh, Physical metallurgy of high-entropy alloys, *JOM J. Min. Met. Mat. S.* 67 (2015) 2254–2261.
- Y.F. Ye, Q. Wang, J. Lu, C.T. Liu, Y. Yang, High-entropy alloy: challenges and prospects, *Mater. Today* 19 (6) (2016) 349–362, <http://dx.doi.org/10.1016/j.mattod.2015.11.026>.
- D.B. Miracle, J.D. Miller, O.N. Senkov, C. Woodward, M.D. Uchic, J. Tiley, Exploration and development of high entropy alloys for structural applications, *Entropy* 16 (2014) 494–525, <http://dx.doi.org/10.3390/e16010494>.
- B. Cantor, Multicomponent and high entropy alloys, *Entropy* 16 (2014) 4749–4768, <http://dx.doi.org/10.3390/e16094749>.
- A. Gali, E.P. George, Tensile properties of high-and medium-entropy alloys, *Intermetallics* 39 (2013) 74–78, <http://dx.doi.org/10.1016/j.intermet.2013.03.018>.
- R.O. Ritchie, The conflicts between strength and toughness, *Nat. Mater.* 11 (2011) 817–822, <http://dx.doi.org/10.1038/nmat3115>.
- M. Seifi, et al., Fracture toughness and fatigue crack growth behavior of as-cast high-entropy alloys, *JOM J. Min. Met. Mat. S.* 67 (2015) 2288–2295, <http://dx.doi.org/10.1007/s11837-015-1563-9>.
- Z. Tang, et al., Fatigue behavior of a wrought  $Al_{0.5}CoCrCuFeNi$  two-phase high-entropy alloy, *Acta Mater.* 99 (2015) 247–258, <http://dx.doi.org/10.1016/j.actamat.2015.07.004>.
- Y. Zang, et al., Microstructures and properties of high-entropy alloys, *Prog. Mater. Sci.* 61 (2014) 1–93, <http://dx.doi.org/10.1016/j.jpmatsci.2013.10.001>.
- G. Laplanche, O. Horst, F. Otto, G. Eggeler, E.P. George, Microstructural evolution of a CoCrFeMnNi high-entropy alloy after swaging and annealing, *J. Alloys Compd.* 647 (2015) 548–557, <http://dx.doi.org/10.1016/j.jallcom.2015.05.129>.
- ASTM Standard E1820, Standard Test Method for Measurement of Fracture Toughness, ASTM International, West Conshohocken, PA, 2014 [www.astm.org](http://www.astm.org).
- C.J. Gilbert, J.M. McNaney, R.H. Dauskardt, R.O. Ritchie, Back-face strain compliance and electrical-potential crack length calibrations for the disk-shaped compact-tension DCT specimen, *J. Test. Eval. (JTEVA)* 22 (1994) 117–120, <http://dx.doi.org/10.1520/jte12644j>.
- ASTM Standard E647, Standard Test Method for Measurement of Fatigue Crack Growth Rates, ASTM International, West Conshohocken, PA, 2013 [www.astm.org](http://www.astm.org).
- K. Haberz, R. Pippin, H.P. Stüwe, Fatigue crack growth in Armco iron at low temperatures, *Proceedings of the 10th Congress on Mater. Test vol. 2*, (1991), pp. 484–488.
- A. Haglund, M. Koehler, D. Catooor, E.P. George, V. Keppens, Polycrystalline elastic moduli of a high-entropy alloy at cryogenic temperatures, *Intermetallics* 58 (2015) 62–64, <http://dx.doi.org/10.1016/j.intermet.2014.11.005>.
- G. Laplanche, P. Gadouad, O. Horst, F. Otto, G. Eggeler, E.P. George, Temperature dependencies of the elastic moduli and thermal expansion coefficient of an equiatomic, single phase CoCrFeMnNi high-entropy alloy, *J. Alloy Compd.* 623 (2015) 348–353, <http://dx.doi.org/10.1016/j.jallcom.2014.11.061>.
- S. Suresh, R.O. Ritchie, A geometric model for fatigue crack closure induced by fracture surface roughness, *Metall. Trans. A* 13A (1982) 1627–1631, <http://dx.doi.org/10.1007/bf02644803>.
- R.O. Ritchie, Mechanisms of fatigue crack propagation in metals, ceramics and composites: role of crack tip shielding, *Mater. Sci. Eng. A* 103 (1998) 15–28, [http://dx.doi.org/10.1016/0025-5416\(88\)90547-2](http://dx.doi.org/10.1016/0025-5416(88)90547-2).
- R. Pippin, K. Haberz, H.P. Stüwe, The plastic deformation of fracture surface contacts in fatigue, *Eng. Fract. Mech.* 53 (3) (1996) 441–448, [http://dx.doi.org/10.1016/0013-7944\(95\)00114-x](http://dx.doi.org/10.1016/0013-7944(95)00114-x).
- S. Suresh, G.F. Zamiski, R.O. Ritchie, Oxide-induced crack closure: an explanation for near-threshold corrosion fatigue crack growth behavior, *Metall. Trans. A* 12A (8) (1981) 1435–1443, <http://dx.doi.org/10.1007/BF02643688>.
- Z.-J. Zhang, et al., Nanoscale origins of the damage tolerance of the high-entropy alloy CrMnFeCoNi, *Nat. Comm.* 6 (2015) 10143, <http://dx.doi.org/10.1038/ncomms10143> Dec. 9.
- T. Niendorf, et al., Fatigue crack growth - microstructure relationships in a high-manganese austenitic TWIP steel, *Mater. Sci. Eng. A* 527 (2010) 2412–2417, <http://dx.doi.org/10.1016/j.msea.2009.12.012>.
- P. Ma, et al., Fatigue crack growth behavior of a coarse- and a fine-grained high manganese austenitic twin-induced plasticity steel, *Mater. Sci. Eng. A* 605 (2014) 160–166, <http://dx.doi.org/10.1016/j.msea.2014.03.035>.
- J.W. Christian, S. Mahajan, Deformation twinning, *Prog. Mater. Sci.* 39 (1995) 1–157, [http://dx.doi.org/10.1016/0079-6425\(94\)00007-7](http://dx.doi.org/10.1016/0079-6425(94)00007-7).
- R.O. Ritchie, Near-threshold fatigue crack propagation in ultra-high strength steel: influence of load ratio and cyclic strength, *J. Eng. Mater. Tech. Trans. ASME Ser. H* 99 (1977) 195–204, <http://dx.doi.org/10.1115/1.3443519>.
- L.W. Tsay, Y.C. Liu, M.C. Young, D.Y. Lin, Fatigue crack growth of AISI 304 stainless steel welds in air and hydrogen, *Mater. Sci. Eng. A* 374 (2004) 204–210, <http://dx.doi.org/10.1016/j.msea.2004.02.018>.
- C. Sarrazin-Baudoux, J. Petit, C. Amzallag, Near-threshold fatigue crack propagation in austenitic stainless steel, *Proceeding of the 12th European Conf. On Fracture (ECF14)*, Cracow, 2002.
- A.-L. Gloane, G. Hénaff, D. Bertheau, P. Belaygue, M. Grange, Fatigue crack growth behaviour of a gamma-titanium-aluminide alloy prepared by casting and powder metallurgy, *Scr. Mater.* 49 (9) (2003) 825–830, [http://dx.doi.org/10.1016/s1359-6462\(03\)00482-2](http://dx.doi.org/10.1016/s1359-6462(03)00482-2).